

Theory of unconventional magnetism in a Cu-based kagome metal

Anja Wenger,¹ Armando Consiglio,² Hendrik Hohmann,¹ Matteo Dürrnagel,^{1,3,*} Fabian O. von Rohr,⁴ Harley D. Scammell,⁵ Julian Ingham,⁶ Domenico Di Sante,⁷ and Ronny Thomale^{1,†}

¹*Institut für Theoretische Physik und Astrophysik and Würzburg-Dresden Cluster of Excellence ct.qmat, Universität Würzburg, 97074 Würzburg, Germany*

²*Istituto Officina dei Materiali, Consiglio Nazionale delle Ricerche, Trieste I-34149, Italy*

³*Institute for Theoretical Physics, ETH Zürich, 8093 Zürich, Switzerland*

⁴*Department of Quantum Matter Physics, University of Geneva, CH-1211 Geneva, Switzerland*

⁵*School of Mathematical and Physical Sciences, University of Technology Sydney, Ultimo, NSW 2007, Australia*

⁶*Department of Physics, Columbia University, New York, NY, 10027, USA*

⁷*Department of Physics and Astronomy, University of Bologna, 40127 Bologna, Italy*

(Dated: November 7, 2024)

Kagome metals have established a new arena for correlated electron physics. To date, the predominant experimental evidence centers around unconventional charge order, nematicity, and superconductivity, while magnetic fluctuations due to electronic interactions, i.e., beyond local atomic magnetism, have largely been elusive. From ab initio design and many-body analysis, we develop a model framework of Cu-based kagome materials the simulations of which reveal unconventional magnetic order in a kagome metal. We find the challenge of locating the appropriate parameter regime for such exotic order to center around two aspects. First, the correlations implied by low-energy orbitals have to be sufficiently large to yield a dominance of magnetic fluctuations and weak to retain an itinerant parent state. Second, the kinematic kagome profile at the Fermi level demands an efficient mitigation of sublattice interference causing the suppression of magnetic fluctuations descending from electronic onsite repulsion. We elucidate our methodology by analyzing the proposed compound CsCu_3Cl_5 , assessing its feasibility for future material synthesis.

Introduction The kagome lattice, characterized by its repeating pattern of corner-sharing triangles, forms a hexagonal network with three distinct sublattices. This unique geometry gives rise to exotic quantum phenomena, rendering it an exclusive host for correlated and topologically nontrivial electronic states. Depending on the balance between electronic interactions and kinetic energy, electronic models on the kagome lattice can yield a myriad distinct physical phases. Kagome compounds with a metallic parent state generically feature intricate non-magnetic phases such as exotic charge orders, nematicity and superconductivity [1–6]. Most extensively discussed is the AV_3Sb_5 family ($A=\text{K,Rb,Cs}$), in which the lack of magnetic order is best explained by both electron-phonon coupling effects [7, 8] and the suppression of on-site Coulomb repulsion due to the sublattice interference (SI) mechanism, preventing local scattering channels between the van Hove singularities (vHS) [9–11]. This leads to a rich zoology of unconventional phases like charge bond (CBO) and loop current orders (LCO), which are largely not found in alternative correlated electron material domains such as cuprate or iron-pnictide compounds [12–14]. Due to the predominance of non-magnetic phases, however, magnetic instabilities that might be unique to kagome kinematics have remained largely unexplored at the microscopic and even at the phenomenological level.

The emergence of magnetic instabilities requires a sufficient degree of electronic correlations. For strong electron-electron interactions, the electrons become Mott-localized on atomic sites, where unpaired spins cre-

ate magnetic moments. The inherent geometric frustration of the kagome lattice leads to unconventional magnetic orders such as spin liquid phases. The most prominent example is Herbertsmithite ($\text{ZnCu}_3(\text{OH})_6\text{Cl}_2$) with an interaction to bandwidth ratio $U/t \approx 20$ [15, 16]. Such materials lie deep in the Mott-insulating regime, rendering the unique features of the kagome bandstructure like vHS and Fermi surface nesting – which drive unconventional charge order in the itinerant case – irrelevant.

In this letter, we aim to fuse the intricacies of electronic kagome kinematics with the potential emergence of magnetic order. We identify kagome materials expected to exhibit correlations intermediate between Herbertsmithite and the weakly correlated AV_3Sb_5 compounds. While Cu-O complexes are likely to be located in the Mott-localized regime, we propose Cu-Cl complexes may strike the aspired compromise between maximum interaction strength while preserving metallicity. Our study further focuses on CsCu_3Cl_5 , a candidate kagome metal consisting of Cu ions, with a minimal set of three low-energy bands. CsCu_3Cl_5 features an isolated mixed-type van Hove singularity (vHS) near the Fermi level, which plays a crucial role for the magnetic fluctuation spectrum resulting in a spin-bond ordered phase. We present a detailed analysis of the electronic structure and magnetic phase diagram, showing that this system provides a realistic platform for investigating exotic magnetic phases in kagome metals.

Model Realization The proposed compound CsCu_3Cl_5 is isostructural with other members of the 135 family, such as AV_3Sb_5 , and crystallizes in the

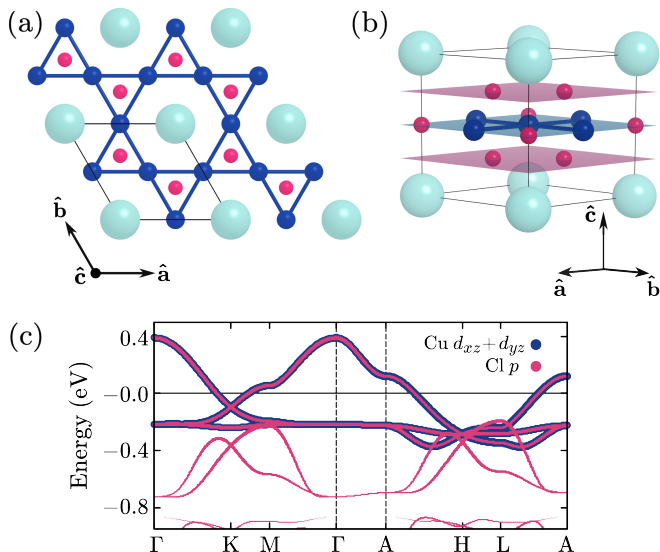


FIG. 1. Crystal structure of the proposed pristine CsCu_3Cl_5 . (a) Top view showing the Cu kagome lattice highlighted by blue bonds. Turquoise, blue and pink spheres represent Cs, Cu and Cl atoms. The unit cell is delimited by black lines. (b) Side view of the unit cell. The blue plane contains the Cu kagome lattice and additional Cl atoms, while the pink planes above and below contain a hexagonal lattice of Cl atoms. (c) Electronic band structure with projected orbital weights featuring distinct kagome bands and an m -type vHS close to E_F .

hexagonal space group $P6/mmm$ (No. 191). It features a two-dimensional kagome network of copper atoms, coordinated octahedrally by chlorine atoms, forming layered Cu_3Cl_5 sheets that are separated along the \hat{c} -axis by a triangular net of cesium ions. CsCu_3Cl_5 exhibits a mixed valence state, where copper ions are present in both Cu(I) and Cu(II) oxidation states, with an average oxidation state of +1.33.

While Cu generally prefers the +II oxidation state, as observed in the chemically related phases Cs_2CuCl_4 [17] and CsCuCl_3 [18], the presence of Cu(I) in compounds such as $\text{Cs}_3\text{Cu}_2\text{Cl}_5$ [19] supports the feasibility of this mixed valence state. A notable point is the possibility of a mixed charge on a crystallographic site. Whether this is statistically distributed in the structural model or whether some form of ordering is present remains an open question. The ionic radii of Cu(I) and Cu(II) in octahedral coordination do not differ significantly, making this mixed occupation proposed here certainly plausible [20]. Due to its full d^{10} electron configuration, Cu(I) lacks the electronic degeneracy needed for Jahn-Teller distortions, making it less prone to such distortions compared to Cu(II). In contrast, Cu(II), with its d^9 electron configuration, is a well-known Jahn-Teller ion and typically undergoes bond elongations or compressions in its octahedral coordination environment to lower its energy [21]. It is also worth noting that Cu(I), at least in chloride environments, does not always form regular coordination

polyhedra. This irregularity might stem from the nature of Cs-Cl compounds, where the large size of Cs ions can sometimes influence the coordination environments of surrounding atoms, though such effects are less likely in layered structures like those in CsCu_3Cl_5 . A detailed analysis of the compound's stability against lattice distortions is provided in the Supplementary Material (SM).

Despite being isostructural to other members of the 135 family like AV_3Sb_5 , the calculated electronic band structure, shown in Fig. 1(c), reveals striking differences to previous reports on known kagome compounds. The characteristic kagome band manifold – including a flat band, a Dirac point located at the K-point, and two vHS at each of the three inequivalent M-points – appears well separated from other bands at low energies. The orbital projection of the bandstructure illustrates that the states at E_F emerge only from the hybridization of the out-of-plane Cu d_{xz} and d_{yz} orbitals with Cl p orbitals. This can be attributed to a collaborative effect: The enhanced valence of Cu (d^9) suggests a single kagome band manifold close to the Fermi level in analogy to ATi_3Bi_5 ($A = \text{Cs, Rb}$) [22, 23], where the d^1 configuration of Ti constitutes the analogue of Cu. In CsCu_3Cl_5 , however, the strong polar Cu-Cl bonding results in an enhanced crystal field splitting, that separates partially filled valence bonds from fully filled bonding and empty anti-bonding states. This is directly reflected in the real space arrangement of chlorine atoms around each copper atom, forming a distorted octahedron, elongated by 0.21 Å towards the center of the hexagonal plaquette (see the SM). Within the octahedra, the spatial proximity of the Cu d -orbitals and Cl p -orbitals induces a pronounced splitting in the d -orbital energy levels. Both effects produce a uniquely isolated and undistorted kagome bandstructure close to the Fermi level. In addition, CsCu_3Cl_5 is distinct from related 135 compounds by its inverted band ordering, with the flat band at the bottom (Fig. 1(c)). This sets an m -type vHS in the vicinity of the Fermi level, opposed to the widely studied p -type variant, with important consequences upon the inclusion of interaction effects.

Analysis of electronic correlations The members of the 135 family are generally considered weakly correlated, where phonons play a crucial role in charge ordering mechanism in collaboration or competition with electronic interactions [24, 25]. To estimate the expected interaction regime for the low energy manifold of CsCu_3Cl_5 , we follow the procedure outlined in Ref. [26]: the degree of electronic correlations in kagome compounds can be understood based on the relative distances between the transition metal atoms, responsible for the electron hopping, and the surrounding ligands, which influence the strength of the crystal field and ligand hybridization. CsV_3Sb_5 , with a ratio of 1.00, has a strong bonding within the kagome layer and small interactions with the surroundings. Herbertsmithite, with a ratio of 1.77, has much weaker bondings between the kagome

sites than bondings towards its ligands, resulting in a strongly interacting kagome network. CsCu_3Cl_5 , characterised by a ratio of 1.25, strikes a balance between electron localization from Cu-Cl bonding, and delocalization due to moderate Cu-Cu distances, positioning it as a potential candidate for hosting both itinerant and localized magnetic phenomena. These considerations are further explicated in the SM. This classification aligns well with the intuitive picture, that a larger filling fraction of the $3d$ shell in copper compared to Ti (d^1) [23], V (d^3) [27] or Cr (d^4) [28] as the central block of the kagome network can enhance local correlations. This general trend seems to be confirmed in CsCr_3Sb_5 with a ratio of 1.02, which is seen to display an admixture of charge and magnetically ordered phases at low temperatures [29, 30].

This higher degree of correlations is further complemented by the expected screening behavior within the kagome bandstructure beyond crystal field effects: firstly, the minimal set of bands in the low energy sector depicted in Fig. 1(c) does not offer scattering channels between vHS of different types [31–33], and reduces the effect of dynamical screening of the bare repulsion by the states close to E_F [34]. Secondly, the m -type character of the vHS reduces the effect of SI [9, 12, 13]. Since two different sublattices contribute to each vHS, the short-ranged Coulomb interaction can still mediate scattering processes between the vHS across the Fermi surface. The correlation strength within the low energy manifold of CsCu_3Cl_5 is therefore anticipated to reside in a sweet spot between that of the weakly correlated CsV_3Sb_5 , and the strongly correlated Herbertsmithite.

Minimal model The isolated nature of the three characteristic kagome bands allows us to capture the electronic structure of CsCu_3Cl_5 around E_F with a single orbital per kagome site. To construct a tight-binding model with maximally localized Wannier functions (MLWF), we begin with an initial approximation using a linear combination of d_{xz} and d_{yz} orbitals. After the spread minimization, three MLWFs are obtained, each centered on a distinct site of the kagome lattice and oriented within the central plane of the coordinating octahedra. These MLWFs share identical shapes, originating from a linear combination of the $d_{x^2-y^2}$ orbital (in the local reference frame of this site) and Cl p -orbitals. Details on the orientations of the local reference frames are provided in the SM. An example MLWF is illustrated in Fig. 2(a),(b) with the orientation of the corresponding octahedron outlined in gray, $\hat{\mathbf{a}}, \hat{\mathbf{b}}, \hat{\mathbf{c}}$ is the (global) reference frame of the crystal, while $\hat{\mathbf{z}}$ aligns with the octahedron axis. The three MLWFs map onto each other under 60° rotation. These orbitals reflect the B_{2g} elementary band representation of $P6/mmm$, well separated from B_{3g} by the pronounced Jahn-Teller distortion described above [35].

By extracting bands from this three-orbital tight-binding model and comparing them with DFT band calculations in Fig. 2(c), we observe a perfect alignment of

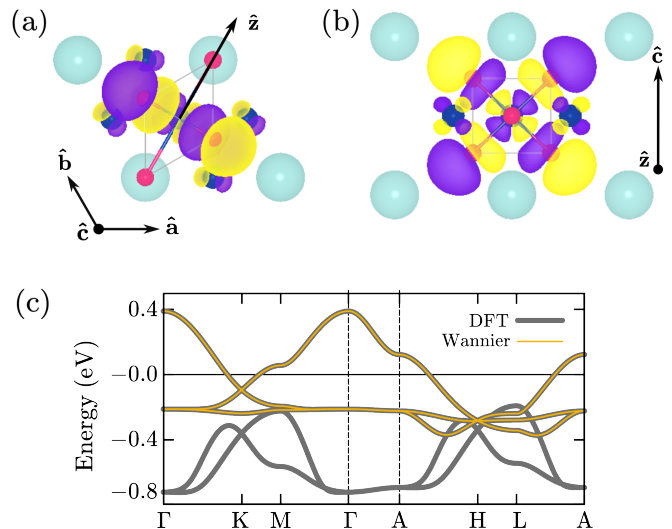


FIG. 2. Wannier orbital centered at the Cu site seen from (a) top and (b) side view. The site-local reference axis $\hat{\mathbf{z}}$ is pointing towards the center of the hexagonal plaquettes. The purple and yellow color of the orbital lobes indicate the phase of the MLWF. (c) Comparison of the DFT band dispersion (gray) with bands obtained from the Wannier three-orbital tight-binding model (yellow).

the bands, combined with a very small spread. This allows for a description using MLWF, making the three-orbital description a simple and well-suited model for many-body calculations.

To study possible instabilities of CsCu_3Cl_5 we equip the non-interacting theory with two particle interactions. Following the discussion of the preceding section and preceding works on the kagome lattice [12, 13, 36], we choose bare interactions consisting of on-site U and nearest-neighbour (NN) repulsion V ,

$$\hat{H}_I = U \sum_{\mathbf{i}} \hat{n}_{\mathbf{i}\uparrow} \hat{n}_{\mathbf{i}\downarrow} + V \sum_{\langle \mathbf{i}, \mathbf{j} \rangle, \sigma \sigma'} \hat{n}_{\mathbf{j}\sigma} \hat{n}_{\mathbf{i}\sigma'}, \quad (1)$$

where $\hat{n}_{\mathbf{j}\sigma} = \hat{c}_{\mathbf{j}\sigma}^\dagger \hat{c}_{\mathbf{j}\sigma}$ is the fermionic number operator on site \mathbf{j} with spin σ . While SI is weakened at the m -type vHS compared to the extensively investigated p -type scenario, it still restricts the accessibility of on-site scattering events on the Fermi surface to a single sublattice for each M -point nesting vector (cf. SM and Ref. [9]). This has striking effects on the nature of the symmetry breaking transition: the partial reduction of onsite interaction U by the imperfect SI at the m -type vHS implies a comparable contribution from local and long range interactions. Hence, V cannot be simply neglected as for e.g. done in Ref. [37].

Many-body analysis of magnetic instabilities The small number of bands crossing the Fermi level and the absence of local degrees of freedom in the Wannierized model make it well-suited for exploring the system's ordering tendencies using numerical many-body methods. We perform functional renormalization group

(FRG) calculations, utilizing the truncated unity implementation provided by the divERGE code base [38]. The FRG provides a well-defined interpolation from the non-interacting model to a low-energy effective theory near the Fermi level by successively integrating out high-energy degrees of freedom [39, 40]. During this RG flow, all quantum fluctuations involving states outside this restricted manifold are incorporated in the screening of the effective two-particle interaction. This is achieved within the FRG by a perturbative expansion of the possible scattering processes, that allows for an unbiased treatment of symmetry breaking transitions in the superconducting, charge, and magnetic channel. This makes FRG a distinguished method for weak to intermediate coupling strengths, *i.e.* the interaction regime suitable for the exploration of itinerant magnetic orders. Further details on the FRG calculations can be found in the SM.

Our FRG analysis reveals a $2 \times 2 \times 1$ magnetic order depicted in Fig. 3, which can be traced to a collaborative effect of two interaction length scales which operate at equal strength for an *m*-type vHS. The on-site U favors the formation of local spin polarization to avoid double occupancy on the sublattice site – this leads to long-range antiferromagnetic order at the Fermi surface nesting vector \mathbf{M}_γ on the sublattice sites γ that do not suffer from SI. Meanwhile, nearest-neighbour V promotes the coupling of adjacent sites and generically favors bond orders over local particle-hole pairs, as known from the *p*-type vHS scenario [9]. This results in a magnetic state $\vec{\Delta}_\gamma = \vec{\Delta}_\gamma^{SDW} + \vec{\Delta}_\gamma^{SBO}$ which combines spin density wave order (SDW)

$$\vec{\Delta}_\gamma^{SDW} \propto \sum_{\mathbf{i}, \mathbf{j}} \cos(\mathbf{i} \cdot \mathbf{M}_\gamma) \langle \hat{c}_{\mathbf{i}\gamma\sigma}^\dagger \vec{\sigma}^{\sigma\sigma'} \hat{c}_{\mathbf{i}\gamma\sigma'} \rangle \quad (2)$$

with finite relative angular momentum components

$$\vec{\Delta}_\gamma^{SBO} \propto \sum_{\langle \mathbf{i}, \mathbf{j} \rangle} \cos(\mathbf{i} \cdot \mathbf{M}_\gamma) \Delta_\gamma^{\mathbf{i}\mathbf{j}\alpha\beta} \langle \hat{c}_{\mathbf{i}\alpha\sigma}^\dagger \vec{\sigma}^{\sigma\sigma'} \hat{c}_{\mathbf{j}\beta\sigma'} \rangle, \quad (3)$$

that constitute a spin bond order phase (SBO). Here, $\langle \mathbf{i}, \mathbf{j} \rangle$ is the sum over unit cell vectors \mathbf{i}, \mathbf{j} such that \mathbf{i}, α and \mathbf{j}, β describe neighboring sites, and all doubly occurring indices are summed over. The real space representations of the SBO order parameter $\Delta_\gamma^{\mathbf{i}\mathbf{j}\alpha\beta}$ are given in the SM.

At the M -point, the associated little group to the point group $P6/mmm$ is given by mmm , which is equivalent to the local symmetry group of the individual kagome sites on the 3f Wyckoff positions. Consequently, the SDW order parameter, which transforms trivially under all elements of mmm , has support only on sublattice γ . In order to mix with the U driven on-site magnetization, the SBO phase transforms within the A_g irreducible representation of mmm and thus represents an extended s -wave magnetization pattern. This is a crucial precondition for the magnetic state to lower its free energy via spin fluctuations of both local and non-local moments

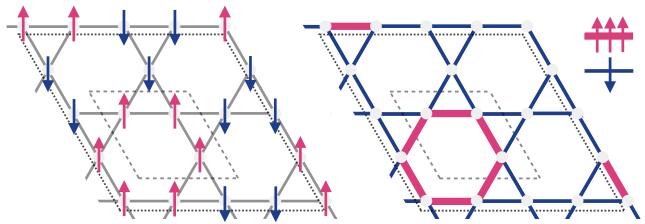


FIG. 3. Magnetic ordering vector of the Cu kagome network as obtained from combined FRG + GL analysis at *m*-type vH filling. The order parameter blends an collinear antiferromagnetic arrangement of local magnetic moments (left) and nearest-neighbor spin bond terms (right), forming a star-of-David pattern. Vanishing net magnetization is preserved.

present in the *m*-type vH scenario. Contrarily, the *p*-type scenario does not allow for a local moment formation at the Fermi level due to SI [9]. While the *p*-type scenario opens up opportunities for bond-magnetization in non-trivial irreducible representations, it also limits the available free-energy gain, since the spin polarization exhibits strong momentum dependence with additional nodes in the quasi-particle spectrum, that cannot contribute from the dominant on-site repulsion U .

A Ginzburg-Landau (GL) analysis (cf. SM) shows that near the onset of magnetic order, the favoured state is a collinear order in which SDW and SBO point along the same axis (Fig. 3), and modulate with a star-of-David pattern. The magnetic arrangement breaks Z_4 translation and spin rotation symmetries, and transforms within the three-dimensional F_2' irrep of the extended C_{6v}''' symmetry group of the enlarged 2×2 unit cell [41]. While retaining the original $P6/mmm$ symmetry, the superposition of the three different A_g states leads to a triple enhancement of the hexagonal bonds compared to the star-like bonds to ensure vanishing net magnetization. This marks the first instance of spontaneous magnetization in kagome metals driven by quantum fluctuations.

Induced spin current order This change of paradigm - from the local moment-driven, to itinerant magnetism - comes with the promise of more, yet unprecedented phases. At lower temperature, deeper in the symmetry-broken phase, higher-order terms in GL expansion of the free-energy become important. In this circumstance, the SDW/SBO configuration may cease to be uniaxial, promoting an octahedral spin configuration, which permits a more intriguing coupling of the order parameter to sub-leading magnetic fluctuations via the spin chirality coupling (cf. SM). For charge-ordered phases, the coupling of real and imaginary bond order is known to promote subsidiary loop current orders [42, 43]; here we draw an interesting parallel to magnetic instabilities. Spin currents are even under time-reversal symmetry (TRS). Hence, a coupling to SBO/SDW order can already appear at first-order in the spin-current order (SCO) parameter via the

cubic term

$$\mathcal{F}^{(3)} \propto \sum_{\alpha\beta\gamma} \varepsilon_{\alpha\beta\gamma} \vec{\Delta}_\alpha^s \cdot (\vec{\Delta}_\beta^s \times \vec{\Delta}_\gamma^{SCO}) \quad (4)$$

where $s = \{SBO, SDW\}$. Minimizing this contribution to the free energy produces a state in which $\vec{\Delta}_\alpha^s \perp \vec{\Delta}_\beta^s \perp \vec{\Delta}_\gamma^{SCO}$, i.e. the $\vec{\Delta}^s$ vectors at the three M points are mutually perpendicular, and locked parallel to the SCO vector, $\vec{\Delta}_\alpha^s \parallel \vec{\Delta}_\alpha^{SCO}$. This locking between spin and M -point is a kind of ‘‘spontaneous spin-orbit coupling’’. Eq. (4) is linear in $\vec{\Delta}^{SCO}$, which implies that non collinear $\vec{\Delta}^s$ is expected to immediately induce SCO, and conversely, the presence of SCO can induce canting of the $\vec{\Delta}^s$ state.

This mechanism for the emergence of spin current appears as a direct consequence of cascading phase transitions characteristic of kagome materials [44]. The only instance of spin currents reported to date is in FeGe, in the A-type AFM phase [45–47]. However, in that system the SCO can be simply viewed as loop current formation of spin-polarized electrons [14, 48, 49]. The new mechanism we describe above gives way to uncharted territory of magnetic states due to the unique features of the kagome lattice, combining the effects of geometric frustration and SI in the moderately coupled regime.

Summary This study explores the emergence of itinerant magnetism in kagome lattice systems. The proposed material candidate CsCu_3Cl_5 displays the three characteristic kagome bands around the Fermi level almost without any interference from additional bands. A description by means of local reference frames enables the identification of a minimal tight-binding model using three maximally localized Wannier orbitals. While many kagome materials exhibit a more complex description, with several vHS near the Fermi level which may interplay to form novel electronic orders [10, 11, 31–33, 50], CsCu_3Cl_5 exhibits an isolated m -type vHS close to the Fermi level, providing a model realization of the kagome Hubbard model.

Our FRG study reveals a unprecedented unconventional $2 \times 2 \times 1$ antiferromagnetic ordering; while kagome magnets have attracted much attention in recent years, the formation of long-range magnetization is usually fostered by dipole interactions of localised magnetic moments rather than an intrinsic electronic mechanism which is at display here [16, 51]. In the presented scenario, quantum fluctuations provide the driving force for the magnetic transition. This expands the catalogue of magnetic states on the kagome lattice: We predict a spin bond order phase with descendent spin current patterns on the kagome lattice, featuring a finite relative angular momentum of the spin-1 particle-hole pair in analogy to spin-0 charge bond order patterns. Our analysis marks the first chapter of emergent magnetic order from itinerant electrons on the kagome lattice, and adds magnetic instabilities to the landscape of symmetry-broken phases in metallic kagome compounds.

Our analysis marks the precedent of an emergent magnetic order from itinerant electrons on the kagome lattice, and sets magnetic instabilities on the landscape of symmetry-broken phases in metallic kagome compounds.

Acknowledgements We thank L.M. Schoop, J.B. Profe, and L. Klebl for valuable discussions and feedback on this work. A.W., M.D., H.H. and R.T. are supported by the Deutsche Forschungsgemeinschaft (DFG, German Research Foundation) through Project-ID 258499086 - SFB 1170, through the Würzburg-Dresden Cluster of Excellence on Complexity and Topology in Quantum Matter - ct.qmat Project-ID 390858490 - EXC 2147, and the research unit QUAST, FOR 5249-449872909 (Project 3). A.C. acknowledges support from PNRR MUR project PE0000023-NQSTI. A.W., A.C., D.D.S. and R.T. acknowledge the Gauss Centre for Supercomputing e.V. (<https://www.gauss-centre.eu>) for funding this project by providing computing time on the GCS Supercomputer SuperMUC-NG at Leibniz Supercomputing Centre (<https://www.lrz.de>) where the DFT and Wannier-based calculations were performed. M.D., H.H. and R.T. are grateful for HPC resources provided by the Erlangen National High Performance Computing Center (NHR@FAU) of the Friedrich-Alexander-Universität Erlangen-Nürnberg (FAU), that were used for the FRG calculations. NHR funding is provided by federal and Bavarian state authorities. NHR@FAU hardware is partially funded by the DFG - 440719683.

Author contributions R.T. initiated and supervised the project. R.T., A.W., A.C., and F.v.R. designed the model system. A.W., A.C. and D.D.S. conducted the first principles calculations and the related Wannier-based analysis. H.H. performed the FRG calculations, that were analysed and interpreted in collaboration with M.D. M.D. carried out the GL analysis with input from H.D.S. and J.I.. All authors contributed to writing the manuscript.

* matteo.duerrnagel@uni-wuerzburg.de

† ronny.thomale@uni-wuerzburg.de

- [1] Y.-X. Jiang, J.-X. Yin, M. M. Denner, N. Shumiya, B. R. Ortiz, G. Xu, Z. Guguchia, J. He, M. S. Hossain, X. Liu, J. Ruff, L. Kautzsch, S. S. Zhang, G. Chang, I. Belopolski, Q. Zhang, T. A. Cochran, D. Multer, M. Litskevich, Z.-J. Cheng, X. P. Yang, Z. Wang, R. Thomale, T. Neupert, S. D. Wilson, and M. Z. Hasan, Unconventional chiral charge order in kagome superconductor KV_3Sb_5 , *Nat. Mater.* **20**, 1353 (2021).
- [2] C. Mielke, D. Das, J.-X. Yin, H. Liu, R. Gupta, Y.-X. Jiang, M. Medarde, X. Wu, H. C. Lei, J. Chang, P. Dai, Q. Si, H. Miao, R. Thomale, T. Neupert, Y. Shi, R. Khasanov, M. Z. Hasan, H. Luetkens, and Z. Guguchia, Time-reversal symmetry-breaking charge order in a kagome superconductor, *Nature* **602**, 245 (2022).

- [3] H. Li, S. Cheng, B. R. Ortiz, H. Tan, D. Werhahn, K. Zeng, D. Johrendt, B. Yan, Z. Wang, S. D. Wilson, *et al.*, Electronic nematicity without charge density waves in titanium-based kagome metal, *Nature Physics* **19**, 1591 (2023).
- [4] Z. Jiang, Z. Liu, H. Ma, W. Xia, Z. Liu, J. Liu, S. Cho, Y. Yang, J. Ding, J. Liu, *et al.*, Flat bands, non-trivial band topology and rotation symmetry breaking in layered kagome-lattice RbTi_3Bi_5 , *Nature Communications* **14**, 4892 (2023).
- [5] P. K. Nag, R. Batabyal, J. Ingham, N. Morali, H. Tan, J. Koo, A. Consiglio, E. Liu, N. Avraham, R. Queiroz, *et al.*, Pomeranchuk instability induced by an emergent higher-order van Hove singularity on the distorted kagome surface of $\text{Co}_3\text{Sn}_2\text{S}_2$, *arXiv preprint arXiv:2410.01994* (2024).
- [6] Y.-X. Jiang, S. Shao, W. Xia, M. M. Denner, J. Ingham, M. S. Hossain, Q. Qiu, X. Zheng, H. Chen, Z.-J. Cheng, *et al.*, Van Hove annihilation and nematic instability on a kagome lattice, *Nat. Mater.* **23**, 1214 (2024).
- [7] Y. Zhong, S. Li, H. Liu, Y. Dong, K. Aido, Y. Arai, H. Li, W. Zhang, Y. Shi, Z. Wang, S. Shin, H. N. Lee, H. Miao, T. Kondo, and K. Okazaki, Testing electron-phonon coupling for the superconductivity in kagome metal CsV_3Sb_5 , *Nat. Commun.* **14**, 1945 (2023).
- [8] Y. Xie, Y. Li, P. Bourges, A. Ivanov, Z. Ye, J.-X. Yin, M. Z. Hasan, A. Luo, Y. Yao, Z. Wang, G. Xu, and P. Dai, Electron-phonon coupling in the charge density wave state of CsV_3Sb_5 , *Phys. Rev. B* **105**, L140501 (2022).
- [9] M. L. Kiesel and R. Thomale, Sublattice interference in the kagome hubbard model, *Phys. Rev. B* **86**, 121105 (2012).
- [10] Y. Hu, X. Wu, B. R. Ortiz, S. Ju, X. Han, J. Ma, N. C. Plumb, M. Radovic, R. Thomale, S. D. Wilson, A. P. Schnyder, and M. Shi, Rich nature of van Hove singularities in kagome superconductor CsV_3Sb_5 , *Nat. Commun.* **13**, 2220 (2022).
- [11] M. Kang, S. Fang, J.-K. Kim, B. R. Ortiz, S. H. Ryu, J. Kim, J. Yoo, G. Sangiovanni, D. Di Sante, B.-G. Park, C. Jozwiak, A. Bostwick, E. Rotenberg, E. Kaxiras, S. D. Wilson, J.-H. Park, and R. Comin, Twofold van Hove singularity and origin of charge order in topological kagome superconductor CsV_3Sb_5 , *Nat. Phys.* **18**, 301 (2022).
- [12] M. L. Kiesel, C. Platt, and R. Thomale, Unconventional fermi surface instabilities in the kagome hubbard model, *Phys. Rev. Lett.* **110**, 126405 (2013).
- [13] W.-S. Wang, Z.-Z. Li, Y.-Y. Xiang, and Q.-H. Wang, Competing electronic orders on kagome lattices at van Hove filling, *Phys. Rev. B* **87**, 115135 (2013).
- [14] J. Zhan, H. Hohmann, M. Dürrnagel, R. Fu, S. Zhou, Z. Wang, R. Thomale, X. Wu, and J. Hu, Loop current order on the kagome lattice (2024), submitted.
- [15] F. Bert, A. Olariu, A. Zorko, P. Mendels, J. C. Trombe, F. Duc, M. A. de Vries, A. Harrison, A. D. Hillier, J. Lord, A. Amato, and C. Baines, Frustrated magnetism in the quantum kagome herbertsmithite $\text{ZnCu}_3(\text{OH})_6\text{Cl}_2$ antiferromagnet, *Journal of Physics: Conference Series* **145**, 012004 (2009).
- [16] M. R. Norman, Colloquium: Herbertsmithite and the search for the quantum spin liquid, *Rev. Mod. Phys.* **88**, 041002 (2016).
- [17] J. A. McGinney, Cesium tetrachlorocuprate. structure, crystal forces, and charge distribution, *Journal of the American Chemical Society* **94**, 8406 (1972).
- [18] A. W. Schlüter, R. A. Jacobson, and R. E. Rundle, A redetermination of the crystal structure of CsCuCl_3 , *Inorganic Chemistry* **5**, 277 (1966).
- [19] S. Hull and P. Berastegui, Crystal structures and ionic conductivities of ternary derivatives of the silver and copper monohalides-II: ordered phases within the $(\text{AgX})_x-(\text{MX})_{1-x}$ and $(\text{CuX})_x-(\text{MX})_{1-x}$ ($M = \text{K, Rb}$ and Cs ; $X = \text{Cl, Br}$ and I) systems, *Journal of Solid State Chemistry* **177**, 3156 (2004).
- [20] R. D. Shannon, Revised effective ionic radii and systematic studies of interatomic distances in halides and chalcogenides, *Foundations of Crystallography* **32**, 751 (1976).
- [21] M. Veidis, G. Schreiber, T. Gough, and G. J. Palenik, Jahn-teller distortions in octahedral copper (II) complexes, *Journal of the American Chemical Society* **91**, 1859 (1969).
- [22] D. Werhahn, B. R. Ortiz, A. K. Hay, S. D. Wilson, R. Seshadri, and D. Johrendt, The kagomé metals RbTi_3Bi_5 and CsTi_3Bi_5 , *Zeitschrift für Naturforschung B* **77**, 757 (2022).
- [23] J. Yang, X. Yi, Z. Zhao, Y. Xie, T. Miao, H. Luo, H. Chen, B. Liang, W. Zhu, Y. Ye, J.-Y. You, B. Gu, S. Zhang, F. Yang, Z. Wang, Q. Peng, H. Mao, G. Liu, Z. Xu, H. Chen, H. Yang, G. Su, H. Gao, L. Zhao, and X. J. Zhou, Observation of flat band, Dirac nodal lines and topological surface states in kagome superconductor CsTi_3Bi_5 , *Nat. Commun.* **14**, 4089 (2023).
- [24] B. R. Ortiz, S. M. L. Teicher, L. Kautzsch, P. M. Sarte, N. Ratcliff, J. Harter, J. P. C. Ruff, R. Seshadri, and S. D. Wilson, Fermi surface mapping and the nature of charge-density-wave order in the kagome superconductor CsV_3Sb_5 , *Phys. Rev. X* **11**, 041030 (2021).
- [25] G. He, L. Peis, E. F. Cuddy, Z. Zhao, D. Li, Y. Zhang, R. Stumberger, B. Moritz, H. Yang, H. Gao, T. P. Devereaux, and R. Hackl, Anharmonic strong-coupling effects at the origin of the charge density wave in CsV_3Sb_5 , *Nat. Commun.* **15**, 1895 (2024).
- [26] M. Jovanovic and L. M. Schoop, Simple chemical rules for predicting band structures of kagome materials, *Journal of the American Chemical Society* **144**, 10978 (2022).
- [27] B. R. Ortiz, S. M. L. Teicher, Y. Hu, J. L. Zuo, P. M. Sarte, E. C. Schueller, A. M. M. Abeykoon, M. J. Krogstad, S. Rosenkranz, R. Osborn, R. Seshadri, L. Balents, J. He, and S. D. Wilson, CsV_3Sb_5 : A \mathbb{Z}_2 topological kagome metal with a superconducting ground state, *Phys. Rev. Lett.* **125**, 247002 (2020).
- [28] Y. Li, Y. Liu, X. Du, S. Wu, W. Zhao, K. Zhai, Y. Hu, S. Zhang, H. Chen, J. Liu, Y. Yang, C. Peng, M. Hashimoto, D. Lu, Z. Liu, Y. Wang, Y. Chen, G. Cao, and L. Yang, Correlated electronic structure and incipient flat bands of the kagome superconductor CsCr_3Sb_5 (2024), *arXiv:2406.03740*.
- [29] Y. Liu, Z.-Y. Liu, J.-K. Bao, P.-T. Yang, L.-W. Ji, S.-Q. Wu, Q.-X. Shen, J. Luo, J. Yang, J.-Y. Liu, C.-C. Xu, W.-Z. Yang, W.-L. Chai, J.-Y. Lu, C.-C. Liu, B.-S. Wang, H. Jiang, Q. Tao, Z. Ren, X.-F. Xu, C. Cao, Z.-A. Xu, R. Zhou, J.-G. Cheng, and G.-H. Cao, Superconductivity emerging from density-wave-like order in a correlated kagome metal (2024), *arXiv:2309.13514*.
- [30] G. Sangiovanni, Superconductor surprises with strongly interacting electrons, *Nature* **632**, 988 (2024).

- [31] H. Li, Y. B. Kim, and H.-Y. Kee, Intertwined van Hove singularities as a mechanism for loop current order in kagome metals, *Phys. Rev. Lett.* **132**, 146501 (2024).
- [32] H. D. Scammell, J. Ingham, T. Li, and O. P. Sushkov, Chiral excitonic order from twofold van hove singularities in kagome metals, *Nat. Commun.* **14**, 605 (2023).
- [33] J. Ingham, A. Consiglio, D. di Sante, R. Thomale, and H. D. Scammell, Theory of excitonic order in scv₆sn₆, *arXiv preprint arXiv:2410.16365* (2024).
- [34] B. R. Ortiz, L. C. Gomes, J. R. Morey, M. Winiarski, M. Bordelon, J. S. Mangum, I. W. H. Oswald, J. A. Rodriguez-Rivera, J. R. Neilson, S. D. Wilson, E. Ertekin, T. M. McQueen, and E. S. Toberer, New kagome prototype materials: discovery of KV₃Sb₅, RbV₃Sb₅, and CsV₃Sb₅, *Phys. Rev. Mater.* **3**, 094407 (2019).
- [35] X. Wu, T. Schwemmer, T. Müller, A. Consiglio, G. Sangiovanni, D. Di Sante, Y. Iqbal, W. Hanke, A. P. Schnyder, M. M. Denner, *et al.*, *Phys. Rev. Lett.* **127**, 177001 (2021).
- [36] J. B. Profe, L. Klebl, F. Grandi, H. Hohmann, M. Dürrnagel, T. Schwemmer, R. Thomale, and D. M. Kennes, The kagome hubbard model from a functional renormalization group perspective (2024), *arXiv:2402.11916 [cond-mat.str-el]*.
- [37] Q.-G. Yang, M. Yao, D. Wang, and Q.-H. Wang, Charge bond order and *s*-wave superconductivity in the kagome lattice with electron-phonon coupling and electron-electron interaction, *Phys. Rev. B* **109**, 075130 (2024).
- [38] J. B. Profe, D. M. Kennes, and L. Klebl, divERGe implements various Exact Renormalization Group examples, *SciPost Phys. Codebases*, 26 (2024).
- [39] W. Metzner, M. Salmhofer, C. Honerkamp, V. Meden, and K. Schönhammer, Functional renormalization group approach to correlated fermion systems, *Rev. Mod. Phys.* **84**, 299 (2012).
- [40] C. Platt, W. Hanke, and R. Thomale, Functional renormalization group for multi-orbital fermi surface instabilities, *Advances in Physics* **62**, 453 (2013).
- [41] J. W. F. Venderbos, Symmetry analysis of translational symmetry broken density waves: Application to hexagonal lattices in two dimensions, *Phys. Rev. B* **93**, 115107 (2016).
- [42] C. Guo, G. Wagner, C. Putzke, D. Chen, K. Wang, L. Zhang, M. Gutierrez-Amigo, I. Errea, M. G. Vergniory, C. Felser, M. H. Fischer, T. Neupert, and P. J. W. Moll, Correlated order at the tipping point in the kagome metal CsV₃Sb₅, *Nat. Phys.* **20**, 579 (2024).
- [43] M. M. Denner, R. Thomale, and T. Neupert, Analysis of charge order in the kagome metal AV₃Sb₅ (*A* = K, Rb, Cs), *Phys. Rev. Lett.* **127**, 217601 (2021).
- [44] H. Zhao, H. Li, B. R. Ortiz, S. M. L. Teicher, T. Park, M. Ye, Z. Wang, L. Balents, S. D. Wilson, and I. Zeljkovic, Cascade of correlated electron states in the kagome superconductor CsV₃Sb₅, *Nature* **599**, 216 (2021).
- [45] J.-X. Yin, Y.-X. Jiang, X. Teng, M. S. Hossain, S. Mardanya, T.-R. Chang, Z. Ye, G. Xu, M. M. Denner, T. Neupert, B. Lienhard, H.-B. Deng, C. Setty, Q. Si, G. Chang, Z. Guguchia, B. Gao, N. Shumiya, Q. Zhang, T. A. Cochran, D. Multer, M. Yi, P. Dai, and M. Z. Hasan, Discovery of charge order and corresponding edge state in kagome magnet FeGe, *Phys. Rev. Lett.* **129**, 166401 (2022).
- [46] X. Teng, L. Chen, F. Ye, E. Rosenberg, Z. Liu, J.-X. Yin, Y.-X. Jiang, J. S. Oh, M. Z. Hasan, K. J. Neubauer, B. Gao, Y. Xie, M. Hashimoto, D. Lu, C. Jozwiak, A. Bostwick, E. Rotenberg, R. J. Birgeneau, J.-H. Chu, M. Yi, and P. Dai, Discovery of charge density wave in a kagome lattice antiferromagnet, *Nature* **609**, 490 (2022).
- [47] X. Teng, J. S. Oh, H. Tan, L. Chen, J. Huang, B. Gao, J.-X. Yin, J.-H. Chu, M. Hashimoto, D. Lu, C. Jozwiak, A. Bostwick, E. Rotenberg, G. E. Granroth, B. Yan, R. J. Birgeneau, P. Dai, and M. Yi, Magnetism and charge density wave order in kagome FeGe, *Nat. Phys.* **19**, 814 (2023).
- [48] S. Han, L. Li, C. S. Tang, Q. Wang, L. Zhang, C. Diao, M. Zhao, S. Sun, L. Tian, M. B. H. Breese, C. Cai, M. V. Milosevic, Y. Qi, A. T. S. Wee, and X. Yin, *Orbital origin of magnetic moment enhancement induced by charge density wave in kagome FeGe* (2024), *arXiv:2407.01076 [cond-mat.str-el]*.
- [49] X. Teng, D. W. Tam, L. Chen, H. Tan, Y. Xie, B. Gao, G. E. Granroth, A. Ivanov, P. Bourges, B. Yan, M. Yi, and P. Dai, Spin-charge-lattice coupling across the charge density wave transition in a kagome lattice antiferromagnet (2024), *arXiv:2404.04459 [cond-mat.str-el]*.
- [50] X. Wu, T. Schwemmer, T. Müller, A. Consiglio, G. Sangiovanni, D. Di Sante, Y. Iqbal, W. Hanke, A. P. Schnyder, M. M. Denner, M. H. Fischer, T. Neupert, and R. Thomale, Nature of unconventional pairing in the kagome superconductors AV₃Sb₅ (*A* = K, Rb, Cs), *Phys. Rev. Lett.* **127**, 177001 (2021).
- [51] J.-X. Yin, B. Lian, and M. Z. Hasan, Topological kagome magnets and superconductors, *Nature* **612**, 647 (2022).
- [52] Webelements, university of sheffield, <https://winter.group.shef.ac.uk/webelements/chlorine/electronegativity.html>, accessed: 16.12.23.
- [53] S. V. Streltsov and D. I. Khomskii, Orbital physics in transition metal compounds: new trends, *Physics-Uspekhi* **60**, 1121 (2017).
- [54] A. Consiglio, T. Schwemmer, X. Wu, W. Hanke, T. Neupert, R. Thomale, G. Sangiovanni, and D. Di Sante, Van Hove tuning of AV₃Sb₅ kagome metals under pressure and strain, *Phys. Rev. B* **105**, 165146 (2022).
- [55] H. LaBollita and A. S. Botana, Tuning the van Hove singularities in AV₃Sb₅ (*A* = K, Rb, Cs) via pressure and doping, *Phys. Rev. B* **104**, 205129 (2021).
- [56] C. Lin, A. Consiglio, O. K. Forsslund, J. Kuspert, M. M. Denner, H. Lei, A. Louat, M. D. Watson, T. K. Kim, C. Cacho, D. Carbone, M. Leandersson, C. Polley, T. Balasubramanian, D. D. Sante, R. Thomale, Z. Guguchia, G. Sangiovanni, T. Neupert, and J. Chang, Giant strain response of charge modulation and singularity in a kagome superconductor (2024), *arXiv:2402.16089 [cond-mat.mtrl-sci]*.
- [57] M. Tuniz, A. Consiglio, G. Pokharel, F. Parmigiani, T. Neupert, R. Thomale, G. Sangiovanni, S. D. Wilson, I. Vobornik, F. Salvador, F. Cilento, D. D. Sante, and F. Mazzola, Strain-induced enhancement of the charge-density-wave in the kagome metal ScV₆Sn₆ (2024), *arXiv:2403.18046 [cond-mat.str-el]*.
- [58] G. Kresse and D. Joubert, From ultrasoft pseudopotentials to the projector augmented-wave method, *Phys. Rev. B* **59**, 1758 (1999).
- [59] G. Kresse and J. Furthmüller, Efficient iterative schemes for ab initio total-energy calculations using a plane-wave

- basis set, *Phys. Rev. B* **54**, 11169 (1996).
- [60] J. P. Perdew, K. Burke, and M. Ernzerhof, Generalized gradient approximation made simple, *Phys. Rev. Lett.* **77**, 3865 (1996).
 - [61] V. Wang, N. Xu, J.-C. Liu, G. Tang, and W.-T. Geng, Vaspkit: A user-friendly interface facilitating high-throughput computing and analysis using vasp code, *Computer Physics Communications* **267**, 108033 (2021).
 - [62] K. Momma and F. Izumi, Vesta: a three-dimensional visualization system for electronic and structural analysis, *Journal of Applied Crystallography* **41**, 653 (2008).
 - [63] A. A. Mostofi, J. R. Yates, Y.-S. Lee, I. Souza, D. Vanderbilt, and N. Marzari, wannier90: A tool for obtaining maximally-localised wannier functions, *Computer Physics Communications* **178**, 685 (2008).
 - [64] D. Di Sante, B. Kim, W. Hanke, T. Wehling, C. Franchini, R. Thomale, and G. Sangiovanni, Electronic correlations and universal long-range scaling in kagome metals, *Phys. Rev. Res.* **5**, L012008 (2023).
 - [65] T. Park, M. Ye, and L. Balents, Electronic instabilities of kagome metals: Saddle points and Landau theory, *Phys. Rev. B* **104**, 035142 (2021).
 - [66] R. Nandkishore, G.-W. Chern, and A. V. Chubukov, Itinerant half-metal spin-density-wave state on the hexagonal lattice, *Phys. Rev. Lett.* **108**, 227204 (2012).
 - [67] C. Xu, S. Wu, G.-X. Zhi, G. Cao, J. Dai, C. Cao, X. Wang, and H.-Q. Lin, Frustrated altermagnetism and charge density wave in kagome superconductor CsCr₃Sb₅ (2023), [arXiv:2309.14812](https://arxiv.org/abs/2309.14812) [cond-mat.supr-con].
 - [68] L. Messio, C. Lhuillier, and G. Misguich, Lattice symmetries and regular magnetic orders in classical frustrated antiferromagnets, *Phys. Rev. B* **83**, 184401 (2011).

Supplementary material

CRYSTAL STRUCTURE

CsCu_3Cl_5 is configured in a $P6/mmm$ space group, with its unit cell defined by the vectors

$$\hat{\mathbf{a}} = (6.025, 0.000, 0.000)$$

$$\hat{\mathbf{b}} = (-3.013, 5.218, 0.000)$$

$$\hat{\mathbf{c}} = (0.000, 0.000, 7.027).$$

The atomic positions within the unit cell are specified in fractional coordinates relative to these vectors and are listed below.

Atom	a	b	c
Cs1	0.000	0.000	0.000
Cu1	0.500	0.500	0.500
Cu2	0.500	0.000	0.500
Cu3	0.000	0.500	0.500
Cl1	0.000	0.000	0.500
Cl2	0.667	0.333	0.736
Cl3	0.333	0.667	0.264
Cl4	0.333	0.667	0.736
Cl5	0.667	0.333	0.264

TABLE I. Atomic positions of CsCu_3Cl_5 in direct coordinates.

CHARGE DISTRIBUTION

To examine the charge distribution within the CsCu_3Cl_5 compound, we must examine the oxidation states of the involved elements. Utilizing the Pauling scale, which spans from 3.98 (Fluorine, the most electronegative) to 0.7 (Francium, the least electronegative), we find that Cs, with an electronegativity of 0.79, typically adopts an oxidation state of +1 in compounds. Conversely, Cl, having an electronegativity of 3.16, predominantly exists in a -1 oxidation state. The transition metal copper, with an electronegativity of 1.9, commonly exhibits oxidation states of +2 and, less common, +1 or +3 [52]. To determine the formal (integer) charges of the atoms in CsCu_3Cl_5 , we distribute (integer) electrons among the unit cell ions to achieve an overall neutral compound. The $6s^1$ electron in cesium is readily relinquished due to its weak binding. Chlorine, requiring only one electron to complete its $3p^6$ configuration, strongly attracts electrons. As a result, we draw four electrons from the three copper atoms. Applying integer charges, two of the Cu atoms are in the less common +1 state, while one is in the +2 state. Given the $P6/mmm$ symmetry of the compound, the choice of which copper atom assumes the +2 state is equivalent, as they can be transformed into each other

through a simple 120° rotation. With three energetically equivalent possibilities for charge distribution, a Lewis resonance can emerge, allowing electrons to hop between the Cu+1 and Cu+2 sites with equal probability. This resonance creates three Cu+2 sites, with two electrons uniformly hopping between them, resulting in a uniform distribution of $-2/3$ per copper site. Consequently, each Cu has an effective charge of $+4/3$. To assess the stability of this charge distribution, an initial magnetic moment imbalance among the Cu atoms is intentionally introduced, followed by relaxation of the electronic degrees of freedom. The outcome consistently reflects the same uniform charge distribution. This suggests that the uniform configuration is not a mere consequence of symmetric initial parameters in the calculations, but rather a stable configuration imposed by the inherent symmetry of the system.

LOCAL FRAME OF REFERENCE

Fig. S1 visualizes the unit cell's three copper atoms (Cu1, Cu2, Cu3) and the orientations of their distorted Cl octahedra within the crystal. The elongated side of the Cl octahedron aligns along $\hat{\mathbf{a}} + \hat{\mathbf{b}}$ for Cu1, $\hat{\mathbf{a}}$ for Cu2, and $\hat{\mathbf{b}}$ for Cu3. We chose a local reference frame for each octahedra such that the elongation observed in pristine CsCu_3Cl_5 is oriented along the $\hat{\mathbf{z}}$ -direction, visualized in Fig. S1 (right). Each octahedron's local reference frame has the Cu atom at the origin, with $\hat{\mathbf{z}}$ along the elongated tips and $\hat{\mathbf{x}}$, $\hat{\mathbf{y}}$ towards the corners.

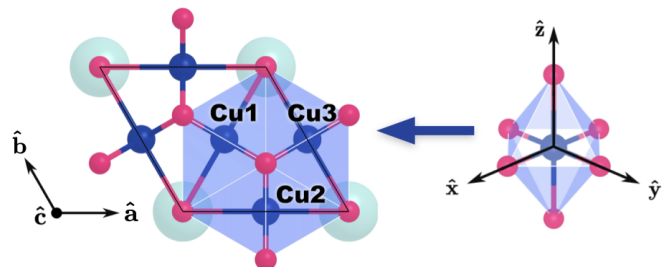


FIG. S1. Top view of the kagome plane (left) highlighting the three copper atoms with the local reference frame around each Cu atom (right).

ELECTRONIC CORRELATIONS ACROSS KAGOME COMPOUNDS

We provide a detailed analysis of the bond ratios for different kagome materials from weak to strong coupling based on the scheme outlined in Ref. [26]:

In weakly correlated CsV_3Sb_5 , the V atoms are coordinated by nearly undistorted Sb-octahedra with a bond

length ratio between neighboring kagome sites ($d(V-V) = 2.75 \text{ \AA}$) and V-ligand distance ($d(V-Sb) = 2.75 \text{ \AA}$) of 1.00. This equal distance between V atoms and their surrounding ligands facilitates significant electron hopping between V sites, leading to more delocalized electrons and weaker correlations. The metallic nature of CsV_3Sb_5 arises from this balance, where interactions between V d-orbitals and Sb p-orbitals are screened, preventing the spontaneous formation of local magnetic moments.

In the strongly correlated Herbertsmithite, each Cu atom is surrounded by a highly distorted octahedron, with four oxygen atoms playing the dominant role in coordination and two Cl atoms contributing less significantly. The distance between neighbouring kagome sites is $d(\text{Cu-Cu}) = 3.53 \text{ \AA}$ while the nearest Cu-ligand distance is $d(\text{Cu-O}) = 1.99 \text{ \AA}$, giving a bond length ratio of 1.77. Chlorine atoms also bond to copper, but at a greater distance of $d(\text{Cu-Cl}) = 2.99 \text{ \AA}$. The close proximity of the oxygen atoms leads to strong Cu-O bonds that confine the electrons, resulting in significant localization. The large Cu-Cu distance weakens electron hopping between kagome sites, while the strong interaction with oxygen atoms further enhances electron localization, driving Herbertsmithite deep into the Mott-insulating regime with strong electronic correlations.

CsCu_3Cl_5 falls between these two cases. The Cu atoms are coordinated by distorted Cl-octahedra, with four equally long bonds out of the kagome plane and two longer bonds in-plane. The Cu-Cu distance is $d(\text{Cu-Cu}) = 3.01 \text{ \AA}$, and the nearest Cu-ligand distance is $d(\text{Cu-Cl}) = 2.40 \text{ \AA}$, giving a bond length ratio of 1.25. This intermediate coordination environment suggests that CsCu_3Cl_5 is likely to exhibit moderate electron correlation. The Cu-Cu distance is longer than in CsV_3Sb_5 but shorter than in Herbertsmithite, allowing for some electron delocalization. At the same time, the weaker Cu-Cl hybridization, compared to the Cu-O bonds in Herbertsmithite, results in reduced electron-electron interactions. This positions CsCu_3Cl_5 between the weakly correlated metallic state of CsV_3Sb_5 and the strongly correlated Mott-insulating state of Herbertsmithite, making it a promising candidate for hosting both itinerant and localized magnetic phenomena.

CRYSTAL DISTORTIONS AND THEIR STABILITY

The complex interplay between electronic structure, orbital ordering and structural dynamics becomes noticeable when analyzing the different structural distortions compatible with the phonon modes of the pristine kagome lattice. This interplay leads indeed to an energy loss known as the Jahn-Teller (JT) effect. The sequence of events remains still uncertain, whether the JT distortion precedes orbital ordering or vice versa [53]. The

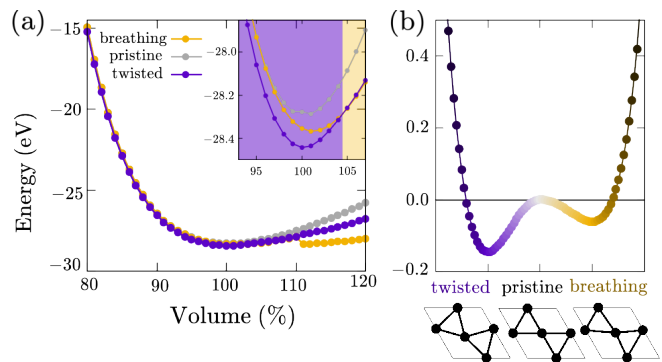


FIG. S2. Energy profiles of the pristine, breathing and twisted configurations for different interpolating geometries and unit cell's sizes. (a) Total free energy as a function of an isotropic change of volume, for all three discussed configurations. The twisted configuration is the most favourable one in a wide range of volume variations. (b) For a unit cell with constant volume, the energy is plotted across varying degrees of interpolation between the pristine and breathing cases, as well as between the pristine and the twisted ones. The twisted configuration stands out as the most energetically favourable.

focus here lies on the breathing and twisted configurations descending from the pristine structure. Fig. S2 illustrates the evolution of the total energy as a function of the geometry, interpolated at constant volume between the pristine and the two distorted cases. The twisted state is the energetically preferred one by ~ 100 meV per unit cell respect to the breathing lattice, and by ~ 150 meV per unit cell respect to the pristine lattice. Finally, we observe that a consistent conclusion is drawn from the analysis of the total free energy F of the three configurations, as a function of an isotropic volume variation, shown in Fig. S2. The twisted case remains the most favourable configuration at least in a $[-5\%, 5\%]$ range around the equilibrium volume, above which a competition with the other phases can be observed. This fact suggests both hydro-static pressure, as well as uni-axial strain, as valid methods for structural and electronic tuning [54–57], whose detailed treatment is beyond the scope of the present work.

Within the twisted kagome configuration, taken as an example, the JT distortion leads to a displacement of the Cu atoms as depicted in Fig. S3(a). Consequently their orbitals become more spatially separated, leading to a reduction in Coulomb repulsion and hybridization and a corresponding decrease in energy. The unit cell's top-view reveals that the Cl ions are still positioned at the center of the Cu triangles, albeit in a twisted triangular arrangement that reduces the number of symmetries. Comparing the band structure of the twisted configuration shown in Fig. S3(b) with the pristine counterpart, the electronic structure of the former demonstrates a reduced dispersion and a slightly lower energy profile. Additionally, the flat band itself exhibits an increased dis-

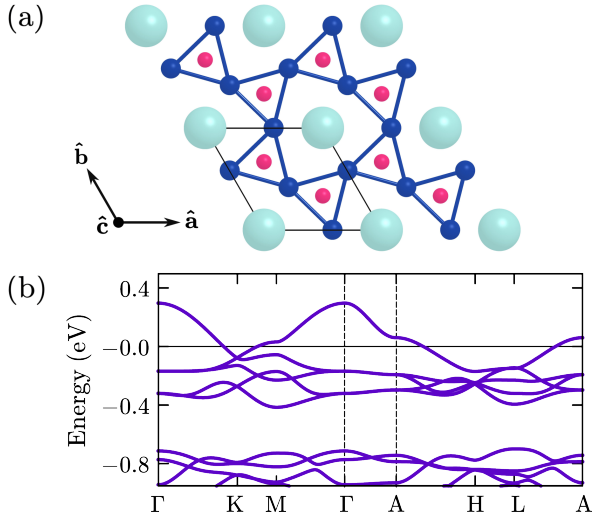


FIG. S3. Twisted configuration of CsCu_3Cl_5 . (a) Top view on the crystal with the Cu kagome lattice highlighted by blue lines. Turquoise, blue and pink spheres represent Cs, Cu and Cl atoms. The unit cell is indicated by black lines. (b) Electronic band structure exhibiting a narrower band width and a closer proximity of the m -type vHS to the Fermi level, in contrast to the pristine configuration.

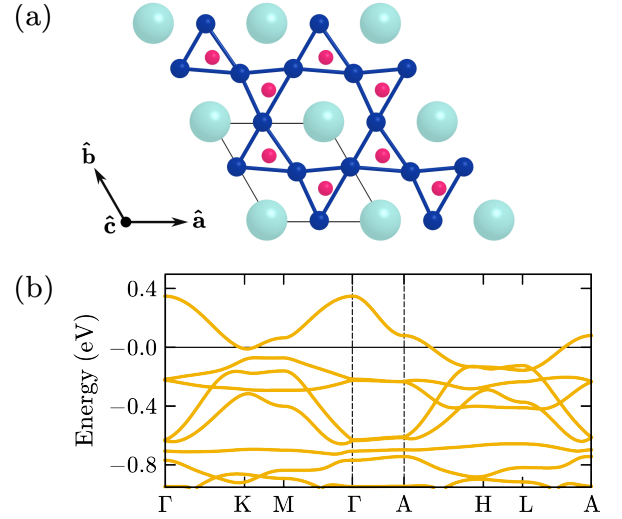


FIG. S4. Breathing configuration of CsCu_3Cl_5 . (a) Top view with the kagome lattice highlighted by blue lines. Turquoise, blue and pink spheres represent Cs, Cu and Cl atoms. The unit cell is indicated by black lines. (b) Electronic band structure of breathing CsCu_3Cl_5 . As the mirror symmetry is broken, the Dirac cone gaps out; the m -type vHS stays close to the Fermi level.

persion due to a reduced destructive interference process among the orbitals of Cu atoms. The Fermi level lies even closer to the (unaffected) m -type vHS than in the pristine case. Given the minimal shift in dispersion, the electronic structure of the twisted configuration remains remarkably close to that of the pristine configuration. Consequently, the minimal model of the pristine configuration can be confidently applied across a broader spectrum.

Another structural disorder compatible with the system's phonon modes is the breathing configuration, depicted in Fig. S4(a). The energy of this breathing kagome lattice is lower than the pristine lattice yet higher than the twisted counterpart. The central observation is a deviation from the previous triangular arrangement, with Cl ions no longer positioned in the center of the Cu triangles. Half of the triangles now possess two long sides and one short side, while the other half exhibit two short sides and one long side. Despite the distortion exhibiting a lower deviation compared to the twisted kagome lattice, it results in an additional reduction in symmetry. As the mirror symmetry is broken, the Dirac cones are no longer preserved and gap out whereas the m -type vHS still remains in the vicinity of the Fermi level.

COMPUTATIONAL METHODS

Density functional theory

Electronic structure calculations were performed with the Vienna Ab Initio Simulation Package (VASP) [58, 59], using the projector augmented wave (PAW) method. Generalized Gradient Approximation (GGA), within the Perdew-Burke-Ernzerhof (PBE) method, has been used to handle exchange and correlation effects [60]. Volume and structural relaxations have been computed with a plane-wave cutoff of 500 eV. The relaxation of the electronic degrees of freedom was considered converged when the energy difference between two steps was equal or smaller than $1.0\text{E-}8$ eV. The ionic relaxation loop was considered converged when the norms of the forces acting on all atoms were equal or smaller than $1.0\text{E-}6$ eV/Å. The number of k -points was set to $18 \times 18 \times 12$, both for relaxation and self-consistent loop. Partial occupancies have been determined according to a Gaussian smearing, with a width of 0.05 eV. Band structures results have been visualized using the VASPKIT postprocessing tool [61], while VESTA [62] has been used to visualize crystal structures and charge density isosurfaces. Wannier models have been constructed by using the WANNIER90 package [63].

Functional renormalization group

The FRG calculations were performed with the TUFGRG backend of the divERGE library [38]. We employed a 30×30 mesh for the bosonic momenta of the vertices, with an additional refinement of 61×61 for the integration of the loop. The form-factor cutoff distance is chosen as 1.99 in units of the lattice vectors. We check for convergence by calculating selected points in parameter space with increased number of momentum points and form-factor cutoff (42×42 , refinement: 81×81 , form-factor cutoff: 3.32). We utilized the Euler 34 integrator of the divERGE library. Taking into account the importance of long range interactions on the kagome, we employ on-site and nearest neighbour density-density interactions via the interaction Hamiltonian Eq. (3) in the main text. The results shown in the main part of this work were obtained with $U = 0.5\text{eV}$ and $V = 0.25\text{eV}$ and are robust against variations in the interaction parameters around the universal interaction values in kagome metals obtained from constrained RPA calculations [64].

THE ROLE OF THE KZ DISPERSION

Due to the layered structure of the compound, we have conducted FRG calculations in the $k_z = 0$ plane, thus omitting the dispersion in the third direction in accordance with other theoretical studies, *e.g.* on AV_3Sb_5 [50]. $CsCu_3Cl_5$ exhibits some hybridization along the k_z direction, introducing out-of-plane dispersion in the band-structure that softens the logarithmic divergence in the density of states at the 2D van Hove points. A future goal is to enhance the two-dimensional characteristics of the layered material by either effectively screening interlayer hopping or by increasing the interlayer spacing between the planes along the z -axis. The latter can be approached in two ways. First, the thickness of the triangular layer can be increased by substituting Cs with a molecule that has a +1 oxidation state, or by adding a neutral molecule to the layer. To preserve the unique kagome physics, it is essential that any added structures maintain kagome symmetry and are carefully examined to ensure that the m -type vHS remain close to the Fermi level. The second approach involves increasing the spacing between the kagome Cu_3Cl layer and the chlorine layers that sandwich it. This can be achieved by substituting the Cl atom at the Wyckoff position 1b with larger elements from the same group, such as Br or I. The k_z dispersion can be measured by the change in energy of the vHS between the M -point ($k_z=0$) and the L -point ($k_z=1/2$). Fig. S5 compares the band structures of $CsCu_3Cl_5$, $CsCu_3Cl_4Br$, and $CsCu_3Cl_4I$. As the size of the substituting atom increases, the kagome bands narrow and shift downward in energy, while the other two bands widen and shift upward. To quantify the effects of

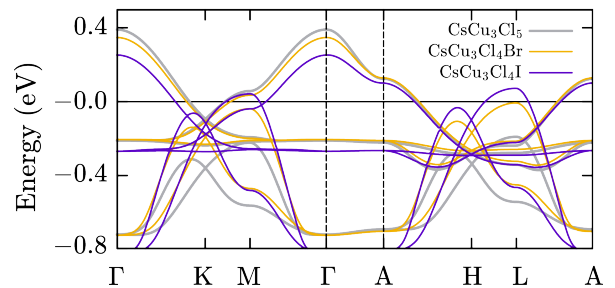


FIG. S5. Comparison of band structures illustrating the effects of increasing substituting atom size on the kagome bands. As the substituting atom size increases, the kagome bands narrow and shift downward in energy, while the other two bands broaden and shift upward.

substitution, Tab. II lists the length of the \hat{c} unit vector perpendicular to the plane, the position of the m -type vHS in the $k_z=0$ plane relative to the Fermi energy, and the change in energy of this vHS from $k_z=0$ to $k_z=1/2$ for the different substitutions. Comparing these values shows that as the substituting atom increases in size, the \hat{c} out-of-plane unit vector indeed grows, decreasing inter-layer hopping and reducing k_z -dispersion. For example, substituting with Iod increases the unit cell size along the \hat{z} -direction from 7.027 \AA to 7.494 \AA and reduces the k_z dispersion of the m -type vHS from 0.26 eV to 0.15 eV . The vHS shifts from 0.06 eV above the Fermi level to 0.04 eV below it. As observed for $CsCu_3Cl_5$, orbital projections show that the three characteristic kagome bands originate from Cu $d_{xz} + d_{yz} + Cl p$ orbitals. The Iod p -orbitals only contribute to the two lower bands in Fig. S5. Projections onto the single Cu atoms confirm the presence of sublattice interference.

Property	$CsCu_3Cl_5$	$CsCu_3Cl_4Br$	$CsCu_3Cl_4I$
$ \hat{c} $ (Å)	7.027	7.179	7.494
$E_{vHS,m}$ (eV)	0.06	0.03	-0.04
$\Delta E_{vHS,m}$ (eV)	0.26	0.22	0.15

TABLE II. Comparison of structural and electronic properties for $CsCu_3Cl_5$, $CsCu_3Cl_4Br$, and $CsCu_3Cl_4I$. $|\hat{c}|$ represents the length of the unit vector perpendicular to the kagome plane, while $E_{vHS,m}$ indicates the energy of the m -type vHS relative to the Fermi level. $\Delta E_{vHS,m}$ denotes its shift in energy from the M -point to the L -point in k -space.

VAN HOVE SCATTERING AT M-TYPE FILLING

The sublattice occupation at the upper van Hove filling is indicated in Fig. S6. At the three inequivalent van Hove points M_γ , the electronic states have equal weight on two of the sublattices and vanishing contribution on the third one. This configuration is known as a mixed m -type van Hove singularity [9]. Hence, scattering events

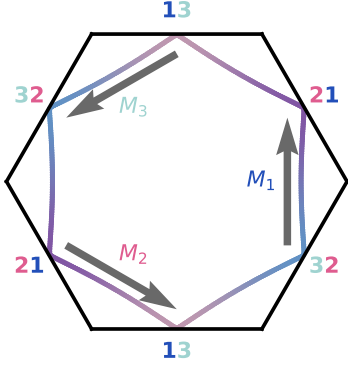


FIG. S6. Fermi surface in the $k_z = 0$ plane for the non-interacting bandstructure at the upper van Hove filling and dominant nesting vectors. The colors indicates the eigenstate contributions on the three different sublattices. At the three M points, *i.e.* the van Hove points, the state is equally composed of the two sublattices as given by the sublattice labels.

with the nesting vector M_γ with $M_\alpha = M_\beta + M_\gamma$ between the vH points can be decomposed into a site local and non-local component

$$\begin{aligned} \langle u(M_\alpha) | \langle u(M_\alpha) | \Gamma_{o_1 o_2 o_3 o_4}(M_\gamma) | u(M_\beta) \rangle | u(M_\beta) \rangle \\ = \Gamma_{\gamma\gamma\gamma\gamma}(M_\gamma) + \Gamma_{\alpha\alpha\beta\beta}(M_\gamma) . \end{aligned} \quad (5)$$

Here, $u(M_\alpha)$ is the eigenstate of the non-interacting Hamiltonian at the vH point M_α and Γ the two-particle interaction. Thereby, the local Hubbard repulsion U can only act on one of the three sublattice sites at a given nesting vector M_γ . This reduces the accessible phase space for the onsite interaction. Likewise, the nearest neighbor interaction V can scatter one sublattice in another ($\alpha \rightarrow \beta$). Thereby, both interaction scales, U and V , operate at similar scales due to the effect of the partial sublattice polarisation of the van Hove points.

In the pure p -type scenario, where every vHS is supported by only a single sublattice, the suppression of the onsite repulsion is stronger manifesting in the absence of phases with local particle-hole pairs at intermediate couplings [12, 13, 36].

GINZBURG-LANDAU ANALYSIS OF THE 3Q ORDER

The FRG calculations exhibit a divergent susceptibility simultaneously at the three inequivalent M - points in the hexagonal Brillouin zone indicating a phase transition with the given wave vector. Solving the linearised gap equation at the phase transition for the three different ordering vectors gives the pattern displayed in Fig. S7, where we only depict the most dominant nearest neighbor bond magnetisation and neglect longer range bonds for clarity. To determine the relative strength of the degenerate ordering vectors, we consider coupling between the

different ordering vectors by means of Ginzburg-Landau (GL) theory at the Fermi level. In contrast to the previously studied 3Q charge orders on the kagome lattice (see *e.g.* Ref. [43]), the relative orientation of the magnetic ordering vector per Q adds three continuous degrees of freedom to the relative strength and sign of the three independent order parameters subject to the GL analysis. To obtain the free energy functional after the FRG flow and avoid double counting, we project the interacting theory at the FRG cutoff scale onto the three van Hove momenta, which carry the dominant spectral weight on the Fermi surface [32, 65]. The prevalent contribution to this Hamiltonian is given by the most divergent part of the FRG vertex, that we expand up to second order in the fluctuations around the static order parameter using a Hubbard-Stratonovich transformation. The resulting action for the low energy effective theory on the Fermi level reads

$$\begin{aligned} S = -T \sum_{\omega_n} \sum_{\alpha s} c_{\alpha s}^\dagger(\omega_n) G_\alpha(\omega_n) c_{\alpha s}(\omega_n) \\ + \sum_{\alpha\beta\gamma} \epsilon_{\alpha\beta\gamma} \vec{\Delta}_\gamma \vec{S}_{\alpha\beta}(\omega_n) + g^{-1} \sum_{\gamma} \vec{\Delta}_\gamma^2 , \end{aligned} \quad (6)$$

with the non-interacting Green's function $G_\alpha(\omega_n) = 1/(i\omega_n - \varepsilon_\alpha)$ and the spin operator $\vec{S}_{\alpha\beta}(\omega_n) = \sum_{ss'} c_{\alpha s}^\dagger(\omega_n) \vec{\sigma}^{ss'} c_{\beta s}(\omega_n)$, where $\vec{\sigma}$ are Pauli matrices acting on spin space, and the sum runs over all fermionic Matsubara frequencies ω_n . Due to the mixed orbital content of the vHS, there is no one-to-one correspondence between the vH index α and the sublattice degree of the original TB model opposed to the p -type scenario [65]. However, the scattering in the magnetic channel is purely off-diagonal in this new basis analogous to the p -type scenario, since the different instabilities $\vec{\Delta}_\gamma = \vec{\Delta}(M_\gamma)$ for $\gamma \in \{1, 2, 3\}$ involve a momentum transfer between the different vHS points at M_α, M_β with $\alpha \neq \beta \neq \gamma$. By carrying out the Gaussian integrals in the remaining Grassman fields, one obtains the free energy

$$F = g^{-1} \sum_{\gamma} \vec{\Delta}_\gamma^2 - \text{Tr} \ln (-\mathcal{G}^{-1}) \quad (7)$$

where we define the fully interacting Green's function $\mathcal{G}^{-1} = G^{-1} + \Sigma^{-1}$ in the tensor product Hilbert space of spin and patch degrees of freedom, *i.e.* $G = 1_{2 \times 2} \otimes \text{diag}(G_1, G_2, G_3)$ and

$$\Sigma = \begin{pmatrix} 0 & \vec{\Delta}_3 & -\vec{\Delta}_2 \\ -\vec{\Delta}_3 & 0 & \vec{\Delta}_1 \\ \vec{\Delta}_2 & -\vec{\Delta}_1 & 0 \end{pmatrix} . \quad (8)$$

Each $\vec{\Delta}_\gamma$ is hence a 2×2 matrix in spin space, whose Pauli vector is kept as tuning parameter. Expanding the free energy in terms of the order parameter fields up to

forth order we obtain the GL functional

$$F = g^{-1} \sum_{\gamma} \vec{\Delta}_{\gamma}^2 + \frac{1}{2} \text{Tr} (G\Sigma)^2 + \frac{1}{4} \text{Tr} (G\Sigma)^4 + \mathcal{O}(\Sigma^6), \quad (9)$$

that is valid in vicinity of the phase transition. The quadratic order

$$F^{(2)} = \sum_{\gamma} \left(\frac{1}{g} - \chi^{ph}(T) \right) \vec{\Delta}_{\gamma}^2 \propto T - T_c, \quad (10)$$

is given by the non-interacting particle-hole susceptibility $\chi^{ph}(T) = \text{Tr}(G_1 G_2)$ and scales linear around the transition temperature T_c . Since the free energy inherits time-reversal and global $\text{SO}(3)$ symmetry of the spin quantisation axis from the kinetic Hamiltonian Eq. (1) in the main text, the cubic term is absent and a coupling of the different order parameter $\vec{\Delta}_{\gamma}$ first appears at quartic order

$$\begin{aligned} F^{(4)} = & Z_1 \left(\sum_{\gamma} \vec{\Delta}_{\gamma}^2 \right)^2 \\ & + 2(Z_2 - Z_1 - Z_3) \left(\vec{\Delta}_1^2 \vec{\Delta}_2^2 + \vec{\Delta}_2^2 \vec{\Delta}_3^2 + \vec{\Delta}_3^2 \vec{\Delta}_1^2 \right) \\ & + 4Z_3 \left((\vec{\Delta}_1 \cdot \vec{\Delta}_2)^2 + (\vec{\Delta}_2 \cdot \vec{\Delta}_3)^2 + (\vec{\Delta}_3 \cdot \vec{\Delta}_1)^2 \right). \end{aligned} \quad (11)$$

The expansion coefficients can be calculated from the kinetic theory on the Fermi level and are given by

$$\begin{aligned} Z_1 &= \text{Tr}(G_1^2 G_2^2), \\ Z_2 &= \text{Tr}(G_1^2 G_2 G_3), \\ Z_3 &= \text{Tr}(G_1 G_2 G_3 G_0). \end{aligned} \quad (12)$$

These prefactors can be calculated analytically by expanding the TB bandstructure around the saddle-points; the resulting action is identical to that of Ref. [66]. While $Z_2 - Z_1 - Z_3 < 0$ results in an equal strength of the three magnetic ordering vectors, $Z_3 < 0$ aligns the magnetisation vectors of the different $\vec{\Delta}_{\gamma}$. This uniaxial spin arrangement of the $3Q$ state persists within the symmetry broken phase as evidenced by the sixth order term $F^{(6)} = -4Z_4 (\vec{\Delta}_1 \cdot \vec{\Delta}_2 \times \vec{\Delta}_3)^2$ with $Z_4 < 0$ [66]. The final result of the combined FRG and GL analysis is presented in Fig. 3 in the main text and resembles other itinerant SDW patterns on the kagome lattice Hubbard model discussed in the literature [12, 13, 38, 65, 67].

The real space order parameter of the parent spin bond order phase determined by our FRG analysis breaks Z_4 translation symmetry and time reversal symmetry \mathcal{T} . Since the global spin quantisation axis remains undefined, the magnetic states can be classified by the irreducible representations (irreps) of the magnetic space group $\mathcal{M} = C_{6v}''' \otimes \mathcal{T}$, that is a direct product of enlarge space group in the 2×2 unit cell and TRS symmetry. The $\vec{\Delta}_{\gamma}^{SDW/SBO}$ obtained by the presented GL analysis transforms within the F_2' irrep, where the prime indicates an odd transformation behaviour under the TRS

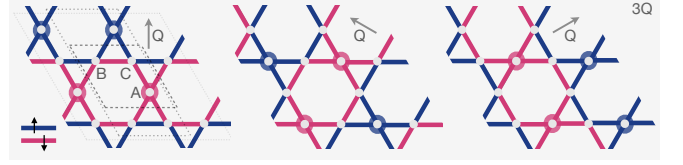


FIG. S7. Three symmetry equivalent magnetic orders with largest susceptibility in the FRG flow. Colored sites (bonds) correspond to a finite local magnetisation on the associated site (bond).

\mathcal{T} . This results from an F_1 structure for the spatial part of the order parameter combined with an odd transformation behaviour of the spin degree of freedom under all mirror operations (corresponding to an A_2 irrep for the spin part). Despite Eq. (11) does not determine the spin polarisation value along the unidirectional quantisation axis, all possible parallel and antiparallel magnetic arrangements of the different $\vec{\Delta}_{\gamma}$ result in the same physical state, potentially translated by one original kagome lattice vector, that constitute the three basis states of the F_2' irrep.

As a direct consequence, the uniaxial spin alignment of the obtained $3Q$ order differs drastically from studies of the kagome Heisenberg model, that suggests an octahedral order as preferred superposition of the different $\vec{\Delta}(M_{\gamma})$ ordering vectors [68]. The reason for this apparent discrepancy roots in the dissimilar nature of the coupling between the 3 ordering vectors: In the kagome Heisenberg model, the different orders interact via the bare short-range first and second nearest-neighbor spin-exchange couplings J_1 and J_2 . In the itinerant picture, however, these couplings are generated dynamically and are driven by bandstructure effects, namely the pronounced nesting of the M -point vHS.

EMERGENCE OF OCTAHEDRAL ORDER INSIDE THE UNIAXIAL MAGNETIC PHASE

Within the symmetry broken phase, the spin exchange coupling is expected to become larger as the GL expansion breaks well below the Néel temperature T_N and eventually promote a perpendicular spin orientation of the different $\vec{\Delta}_{\gamma}$ in accordance with self-consistent mean field calculations on the honeycomb lattice [66]. This tendency can be directly inferred from the highest order GL term considered above: Exploiting the universal relation $|\vec{\Delta}_{\gamma}|_{T=0} \propto T_N$, we can reevaluate the prefactors Z_i of the GL functional at low temperatures in the limit $T_N \lesssim t$ with t is the kinetic energy scale of the system to obtain an intuition of the leading coupling terms between the magnetic ordering vectors. We recognize, that Z_4 changes sign already at small values of T_N , thus favoring an pairwise orthogonal orientation of the magnetic vec-

tors $\vec{\Delta}_\alpha \perp \vec{\Delta}_\beta \perp \vec{\Delta}_\gamma \perp \vec{\Delta}_\alpha$ [66]. We thus recover the octahedral spin order deep inside the magnetic phase, that is separated from the uniaxial F'_2 order by a first order

transition. As discussed in the main text, the non uniaxial spin order couples linearly to spin loop current order, immediately inducing a coexisting spin current order.